



Cell structure, stiffness and permeability of freeze-dried collagen scaffolds in dry and hydrated states



M.C. Varley^a, S. Neelakantan^a, T.W. Clyne^b, J. Dean^b, R.A. Brooks^c, A.E. Markaki^{a,*}

^a Department of Engineering, Cambridge University, Trumpington Street, Cambridge CB2 1PZ, UK

^b Department of Materials Science & Metallurgy, Cambridge University, 27 Charles Babbage Road, Cambridge CB3 0FS, UK

^c Division of Trauma & Orthopaedic Surgery, Addenbrooke's Hospital, Hills Road, Cambridge CB2 2QQ, UK

ARTICLE INFO

Article history:

Received 1 October 2015

Received in revised form 22 December 2015

Accepted 27 January 2016

Available online 28 January 2016

Keywords:

Collagen scaffolds

Cell structure

Cell interconnectivity

Specific surface area

Young's modulus

Specific permeability

ABSTRACT

Scaffolds for tissue engineering applications should be highly permeable to support mass transfer requirements while providing a 3-D template for the encapsulated biological cells. High porosity and cell interconnectivity result in highly compliant scaffolds. Overstraining occurs easily with such compliant materials and can produce misleading results. In this paper, the cell structure of freeze-dried collagen scaffolds, in both dry and hydrated states, was characterised using X-ray tomography and 2-photon confocal microscopy respectively. Measurements have been made of the scaffold's Young's modulus using conventional mechanical testing and a customised see-saw testing configuration. Specific permeability was measured under constant pressure gradient and compared with predictions. The collagen scaffolds investigated here have a coarse cell size (~ 100 – $150\ \mu\text{m}$) and extensive connectivity between adjacent cells (~ 10 – $30\ \mu\text{m}$) in both dry and hydrated states. The Young's modulus is very low, of the order of 10 kPa when dry and 1 kPa when hydrated. There is only a single previous study concerning the specific permeability of (hydrated) collagen scaffolds, despite its importance in nutrient diffusion, waste removal and cell migration. The experimentally measured value reported here ($5 \times 10^{-10}\ \text{m}^2$) is in good agreement with predictions based on Computational Fluid Dynamics simulation and broadly consistent with the Carman–Kozeny empirical estimate. It is however about three orders of magnitude higher than the single previously-reported value and this discrepancy is attributed at least partly to the high pressure gradient imposed in the previous study.

Statement of Significance

The high porosity and interconnectivity of tissue engineering scaffolds result in highly compliant structures (ie large deflections under low applied loads). Characterisation is essential if these scaffolds are to be systematically optimised. Scaffold overstraining during characterisation can lead to misleading results. In this study, the stiffness (in dry and hydrated states) and specific permeability of freeze-dried collagen scaffolds have been measured using techniques customised for low stiffness structures. The scaffold cell structure is investigated using X-ray computed tomography, which has been applied previously to visualise such materials, without extracting any structural parameters or simulating fluid flow. These are carried out in this work. 2-photon confocal microscopy is used for the first time to study the structure in hydrated state.

© 2016 Acta Materialia Inc. Published by Elsevier Ltd. This is an open access article under the CC BY license (<http://creativecommons.org/licenses/by/4.0/>).

1. Introduction

In tissue engineering, a highly porous permeable scaffold is required to provide appropriate void space for mass transport, for neovascularisation and to act as a template for de novo tissue

formation. Many (natural and artificial) scaffolds are based on a collagenous matrix – collagen is the most abundant protein in the extracellular matrix – and they have a number of attractive features [1–5]. However, collagen is a particularly challenging material to fabricate into fine structures, due to its hydrophilicity. Freeze-drying is a well-established method for producing collagen-based scaffolds with architectures complementary to tissue engineering applications [6]. These collagen scaffolds have

* Corresponding author.

E-mail address: am253@cam.ac.uk (A.E. Markaki).

Table 1
Summary of the characterisation techniques employed for collagen-GAG scaffolds.

Characteristic	Technique	References
Scaffold architecture	Optical microscopy	[11,14,16,18,22]
	Scanning electron microscopy	[16,18]
	X-ray computed tomography	[16,18]
Young's modulus	Compression	[12–14,16,17,21–24]
	Tension	[12]
Permeability	Pressure gradient and flow rate measurement	[12,16]
	Numerical prediction	[10,22]

often been combined with glycosaminoglycans (GAGs), which are also constituents of the extracellular matrix. They have been found to promote angiogenesis and reduce foreign body reactions [7]. Collagen scaffolds have been characterised in various ways in both dry and wet (hydrated) states, although of course they are always hydrated *in vivo*. They can be termed “cellular”, meaning that their structures are divided up into cells of some sort.

A summary of the techniques employed for characterising the cell architecture, stiffness (Young's modulus) and permeability of collagen-GAG freeze-dried scaffolds is shown in Table 1. The scaffold structure, particularly the *cell architecture*, is very important, since it can influence both the biological response [8–11] and the mechanical and transport properties [12–17]. The cell structure can be manipulated by varying the freeze-drying conditions. For example, by varying the freezing temperature, the cell size can be tailored [18]. Introducing thermal gradients during the freezing process can lead to anisotropic cell structures [8,19,20], and hence affect biological cell organisation and scaffold properties. The cross-linking method [14,21] has also been found to affect significantly the Young's modulus of the scaffold and biological cell response. Cross-linking typically involves either a physical dehydrothermal-based (DHT) or a chemical, carbodiimide-based (EDAC) process.

Measured [12,13,16,21–24] Young's moduli of freeze-dried (wet and dry) scaffolds tends to be very low – typically ~1–40 kPa, with values usually towards the lower end of the range when wet (hydrated) and larger when dry. The main reason for (all) values being so low (i.e. orders of magnitude below those typical of rubbers), apart from the very high porosity level (often ~95–99%), is that elastic deformation occurs primarily via bending of slender structural elements, such as cell walls. This allows large deflections under low applied loads – i.e. generates a low stiffness – and this is the basis of many types of (highly compliant) fibre network material [25–33]. (There is, however, always the possibility of some kind of inelastic deformation occurring, as a result of plasticity or damage in the cell walls, giving an anomalously low stiffness: it is essential when measuring such stiffness to check that the deformation is genuinely reversible.)

Permeability is also a strong function of porosity level and pore architecture, particularly the pore connectivity. It is also very sensitive to structural scale. (While stiffness can have a dependence on scale, particularly for bending-dominated deformation, in general this is much weaker than for permeability.) There is also a more complex dependence on cell architecture, since the tortuosity of individual channels, and possible existence of high flow rate paths, can also affect the measured permeability. Furthermore, the permeability of a biological structure, such as a scaffold, can play an important role in its performance, affecting nutrient and oxygen diffusion, waste removal, and cell migration into the scaffold [34–38]. Of course, the resistance to fluid flow increases as the channels become finer. Scale is most commonly characterised via the specific surface area (area per unit volume), S . Actually, very few biological studies appear to have focused on the value of S in

the context of permeability despite the fact that it features in the most commonly-used (empirical) relationship between the specific permeability, κ , and the pore architecture, which is the Carman–Kozeny equation [39]

$$\kappa = \frac{p^3}{\lambda(1-p)^2 S^2} \quad (1)$$

where p is the porosity level and λ is a dimensionless constant, often taken to have a value ~5.

Rather surprisingly in view of its significance, there are relatively few experimentally-measured values reported in the literature for the specific permeability of scaffolds of this type. Furthermore, the values that have been reported cover a wide range, and some are very small indeed. The only data relating to collagen scaffolds of the type being investigated here appears to be that of O'Brien and co-workers [10], who reported values in the vicinity of 10^{-13} m^2 . This is a very low permeability, particularly in view of the fact that it relates to a cell structure that is relatively coarse and appears to be fairly open and inter-connected.

In the present paper, the cell structure of freeze-dried collagen scaffolds is investigated, in both dry and hydrated states, and measurements are made of their Young's modulus (E) and specific permeability (κ). Efforts are made to minimise the sample strain during these measurements, since excessive straining occurs easily with such highly compliant material and can produce misleading results. The inertia of the testing equipment is determined by the mechanical linkage system that is to be moved. In conventional testing machines, such effects can be significant. A customised see-saw set-up allowing such effects to be minimised has been designed here. The cell size and connectivity, and specific surface area of the scaffolds are explored using X-ray computed tomography. This technique has only been applied previously to such materials to visualise their architecture, without extracting any structural parameters or simulating deformation or fluid flow: all of these operations are carried out in the present work. To study the structure in hydrated state and approximate the *in vivo* situation, 2-photon confocal microscopy, involving laser-excited fluorescence and second harmonic signals, is used.

2. Materials and methods

2.1. Scaffold fabrication

The collagen-glycosaminoglycan (GAG) suspension was fabricated using a previously-described protocol [11]. All chemicals were obtained from Sigma Aldrich. Insoluble type I collagen (0.5 wt%) and chondroitin sulphate salts (0.05 wt%) were suspended in 0.05 M acetic acid and homogenised at 15,000 rpm using a T81 UltraTurrax homogeniser (IKA, Germany). The suspension was poured into an aluminium mould and sealed in place. The mould suspension was then freeze-dried (Virtis advantage, SP Industries, USA), by cooling to -40°C at a rate of $-0.9^\circ\text{C min}^{-1}$, held for 60 min and then sublimated under a vacuum of 50 mTorr at 0°C for 17 h. Subsequently, the scaffold was cross-linked in a 48-well tissue culture plate for 4 h, using the chemical 1-ethyl-3-(3-dimethyl aminopropyl) carbodiimide (EDAC), alongside the catalyst N-hydroxysuccinimide (NHS) at a molar ratio of 2.5 M EDAC/M NHS. The cross-linking solution had a concentration of 6 mM EDAC per gram of collagen.

2.2. Scaffold characterisation

2.2.1. Relative density measurement (of dry samples)

The relative density of the collagen-GAG (termed CG) scaffold, ρ^*/ρ_s , was calculated from the dry density of the CG scaffold after

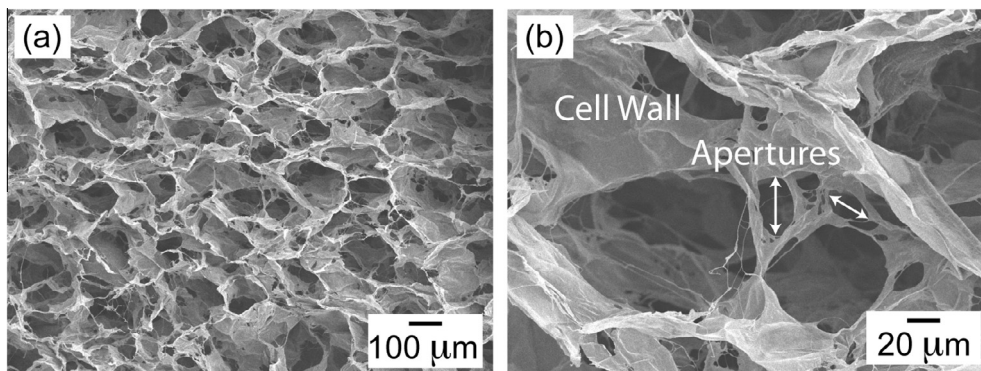


Fig. 1. Typical SEM micrographs of a section through a (dry) CG scaffold.

freeze drying (ρ^*) and the known [11] dry density of solid collagen ($\rho_s = 1.3 \text{ Mg m}^{-3}$). The GAG was assumed to have a minimal contribution. The scaffold diameter and height were measured using a Keyence® dual-axis laser micrometer (model: TM-040, resolution of $\pm 3 \text{ } \mu\text{m}$).

2.2.2. SEM (of dry samples)

Scanning electron microscopy (SEM), X-ray computed tomography (CT) and 2nd harmonic 2-photon imaging were used to investigate the scaffold cell structure. For SEM, the scaffolds were sliced with a scalpel, before being hydrated and freeze dried again, to ensure that the cells were not deformed. The scaffolds were then mounted, gold sputter-coated and imaged, using a Jeol-5800 SEM in secondary mode. These SEM images were thresholded, using a customised Matlab code, and the centre of each cell was computed. An ellipse-fit method was used and an equivalent cell diameter obtained, using an equivalent iso-volume sphere. About 250 cells were analysed. Fig. 1 shows typical SEM images at different magnifications, illustrating the pronounced “cellular” structure and a wide range of apertures (gaps) in the cell walls. The cell wall thickness appears to be of the order of $1 \text{ } \mu\text{m}$.

2.2.3. X-ray computed tomography (of dry samples)

For CT, two samples (10 mm diameter, 10 mm height) were punched from larger scaffold sheets, designated as CG-1 and CG-2. Tomography scans, with $3.4 \text{ } \mu\text{m}$ linear resolution (voxel resolution $3.4 \times 3.4 \times 3.4 \text{ } \mu\text{m}^3$), were acquired using a General Electric Phoenix X-ray Nanotom m system (GE Sensing & Inspection Technologies GmbH, Munich, Germany) equipped with a sub-micron focal spot X-ray source. The source voltage and current were set at 80 kV and 150 μA . A Mo target was used. The scans were recorded at projection angles between 0° and 360° , in steps of 0.2° . To increase the signal to noise ratio, 4 frames were captured and averaged for each projection on a 7.2 megapixel 14-bit detector array. To avoid edge effects, a sub-volume of $4 \times 4 \times 4 \text{ mm}^3$ was analysed and, within this volume, 15 sub-sections ($683.4 \times 683.4 \times 683.4 \text{ } \mu\text{m}^3$) were analysed. These data were imported into myVGL2.2 (Volume Graphics GmbH), to divide the CT data into an image stack for further analysis.

2.2.4. 2-Photon (3-D) confocal microscopy (of hydrated samples)

For the 2-photon work, four samples (5 mm diameter, 4 mm height) were punched from larger scaffold sheets. From each sample, one sub-volume of $1200 \times 1200 \times 250 \text{ } \mu\text{m}^3$ (length, width and thickness respectively) was analysed. The samples were suspended in distilled water and imaged using a LaVision BioTec TriM Scope II system with an Insight DeepSee dual-line tunable laser equipped with a $25\times$ water-immersion lens with a numerical aperture of 1.05. The laser was tuned to 880 nm and a power of 50 mW, to cause excitation of the 2nd harmonic of the collagen. The reading

was obtained using a red-enhanced GaAsP detector, after the response was low pass filtered to allow collection of wavelengths below 510 nm. To increase the signal to noise ratio, the images were line-averaged twice. Voxel resolution was $3.13 \times 3.13 \times 3.13 \text{ } \mu\text{m}^3$.

2.2.5. Analysis of CT and 2-photon images

CT and 2-photon datasets were analysed as follows. First, median filtering was applied to smooth the 3-D images, using a $3 \times 3 \times 3$ kernel. The image stack was thresholded, using a customised Matlab program. To threshold the CT data, a threshold level was defined to give a 99.5% porous structure as calculated from experimental measurements. Any voxels of intensity below the threshold were assumed to represent void space whereas those above were scaled so the varying intensity of pixel represented the varying density of collagen. Fully saturated voxels represented 100% dense collagen whereas those just above the threshold level represented only 1% dense collagen. 3-D cells were objectified using a voxel-growth constrained algorithm (Avizo Fire 3-D software). Each individual cell was then imported into Matlab, to calculate the cell volume, which was converted to an effective diameter using an equivalent iso-volume sphere. Fig. 2(a)–(c) show respectively a typical 2D tomographic reconstruction before and after thresholding, and after cell fitting. Comparing the cell-fitted structure to the original one, estimates of the cell interconnectivity (aperture size) were made. This involved working out the length (in μm) of each cell boundary and approximating it to a circular aperture – see Fig. 2(c). (Because of the image processing that has been carried out to clarify the cell structure, the cell walls appear thicker than they actually are.)

2.2.6. Specific surface area

The scale of the structure was characterised via the specific surface area, S , which was measured using a Brunauer–Emmett–Teller (BET) gas adsorption isotherm method on an ASAP 2020 Porosimeter (Micromeritics Instrument Co, Norcross, USA). Four scaffolds were sliced from a cast sheet, to give an approximate weight of around 0.2 g. The samples (scaffolds) were then re-suspended and washed in distilled water before re-freeze drying under the previously described protocol to give an undeformed clean sample. The sample was then placed into a long neck, round bottom sample tube and loaded into sample ports and evacuated to a high vacuum (2 μmHg). Nitrogen adsorption measurements were taken at 77 K, up to a pressure of 230 mmHg (pressure of 0.3 bar).

Estimates of S were also obtained from 3-D tomographic and 2-photon confocal reconstructions. The CT and 2-photon images obtained were thresholded, as described in Section 2.2.5, and converted to a 3-D surface reconstruction using Avizo Fire (version 7.0). The total surface area of the scaffold was then measured and converted to a specific surface area (in m^{-1}) by dividing by the total scaffold volume (scaffold plus void space).

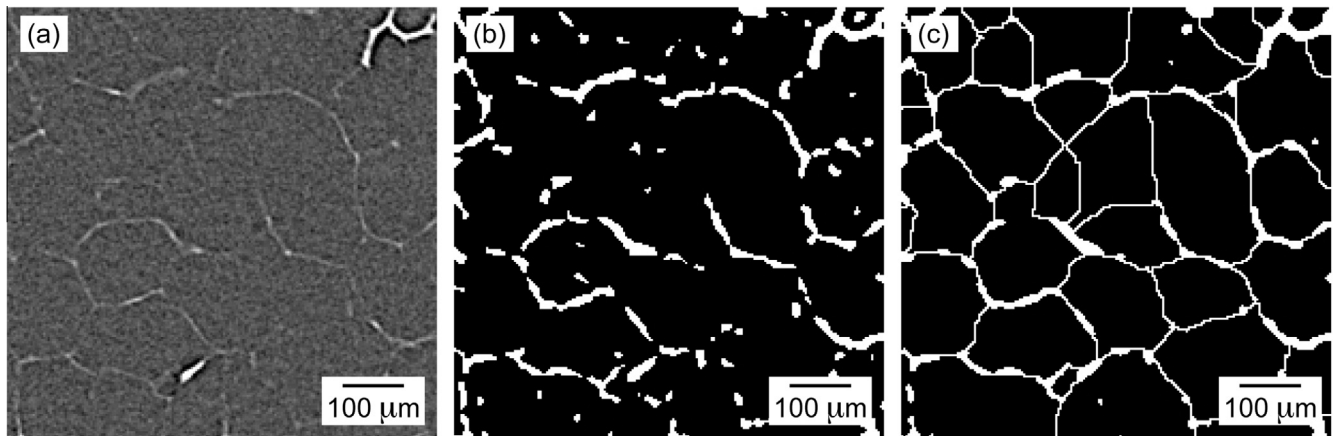


Fig. 2. (a) 2D tomographic reconstruction showing a section through the CG scaffold. Corresponding images (b) after thresholding and (c) cell fitting procedure using a voxel-growth constrained algorithm within Avizo Fire Version 7.

2.3. Mechanical testing

2.3.1. Conventional testing

Cylindrical samples freeze-dried to dimensions of 7 mm (height) \times 9 mm (diameter) were used for compressive testing. Compressive stress–strain curves were obtained using a screw-driven desktop Instron machine, fitted with a 5 N load cell. Three samples were tested in both dry and hydrated conditions. Tests were carried out under displacement-control, at a strain rate of $\sim 10^{-4} \text{ s}^{-1}$. Displacement was measured using a Keyence® bi-axial laser micrometer. In the hydrated condition, scaffolds were immersed in Phosphate Buffer Solution (PBS) for 24 h, to ensure full hydration, and then remained immersed through testing. The through-thickness Young's modulus was measured from the tangent slope of the unloading stress–strain curve (within the elastic regime). Four samples were tested in both dry and hydrated conditions, from which the average value was taken and standard deviation calculated.

2.3.2. See-saw testing

A customised “see-saw” set-up, with a lower inertia compared to a standard Instron machine, has been designed to measure the through-thickness Young's modulus of the scaffolds – see Fig. 3. The set-up has a central pivot resting on a frictional support base

that perfectly balances the free extending arms on either side. The end of one arm is fixed, with a small container to hold the liquid and transfer the load into the collagen sample aligned beneath a flat loading platen. Counter-weights are added in the hanging basket fixed to the other arm, in order to balance the arms such that the loading platen touches the sample surface. The load was ramped up at a constant rate of $\sim 10^{-4} \text{ N s}^{-1}$, by pumping liquid (via a peristaltic pump) into the container. The resulting displacement was monitored using a Keyence® bi-axial laser micrometer. Four samples from each condition (dry and hydrated) were tested, from which the average value was taken and standard deviation calculated.

2.4. Permeability measurement

Various methods have been used by other workers [40] to assess the permeability of biological structures. Specific permeability was measured in the current work using a constant pressure gradient method. The experimental set-up is depicted in Fig. 4. The rig allows small pressure differences to be imposed across the scaffold, defined by the hydrostatic head of water ($\Delta P = \rho h g$), since the bottom of the scaffold is exposed to the atmosphere. The pressure was held constant across the scaffold (thickness L) and the volumetric flow rate (Q) of distilled water through the scaffold

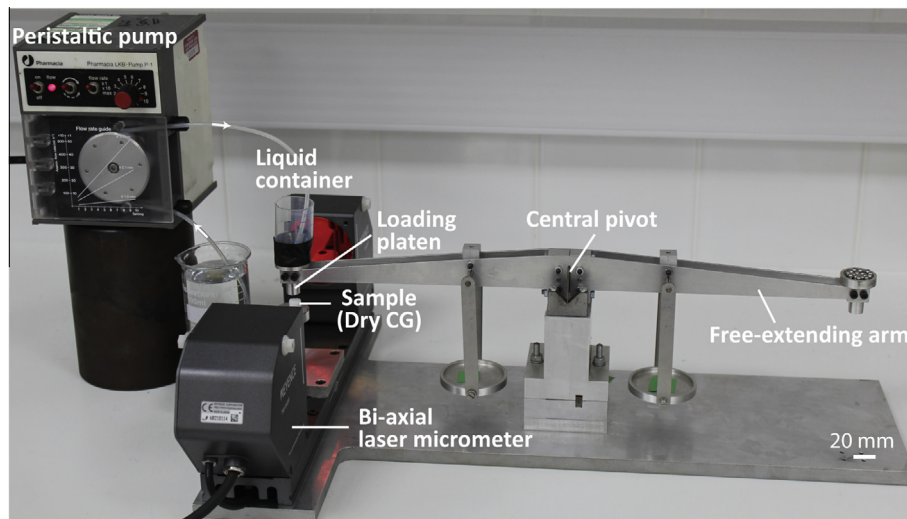


Fig. 3. See-saw set-up for measuring the through-thickness Young's modulus of the scaffolds.

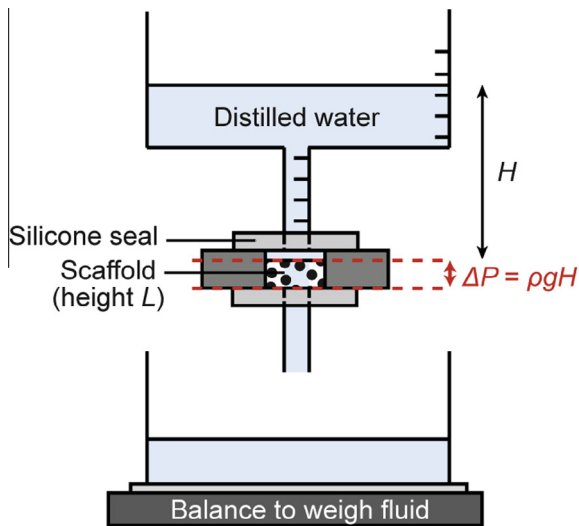


Fig. 4. Schematic of the set-up employed for measuring scaffold permeability.

was measured (from the mass of water passing through the scaffold in a given time). This mass was measured, using a Mettler PE 360 balance with a precision of 1 mg, and converted to volumetric flow using the fluid density ($\rho = 0.998 \text{ Mg m}^{-3}$). From Q , the sectional area (A) and the pressure gradient, $\Delta P/L$, the specific permeability, κ , was calculated using Darcy's Law

$$\kappa = \eta \frac{Q}{A} \frac{L}{\Delta P} \quad (2)$$

in which η , the dynamic viscosity, has units of Pa s and κ has units of m^2 . The viscosity of the water was taken as $8.9 \times 10^{-4} \text{ Pa s}$. A total of 10 samples (5 mm diameter, 3 mm height) were used and three repeat measurements were made on each sample. The pressure gradients created in the samples during these experiments were all about 10 Pa mm^{-1} , which is considerably lower than in many such experiments. Furthermore, a press-fit mount was used to prevent scaffold deformation. The mount aperture was slightly larger than the scaffold diameter in the dry state. When hydrated, the scaffold expanded to fill the entire aperture.

2.5. Tomographic capture and modelling of liquid flow

Collagen scaffolds were scanned using a Skyscan 1172, high resolution desktop μCT scanner with a resolution of 810 nm. 3-D cell and scaffold structures were rendered from (serial section) X-ray radiographs, using the Simpleware ScanIP software suite and built-in segmentation tools. A typical visualisation is shown in Fig. 5(a).

The +FE module of the ScanIP software was used to mesh the cell volume, using about 32 million first order tetrahedral elements. The +FLOW module was then used to calculate the permeability of the scaffold, using a built-in Stokes solver (based on laminar flow). Boundary conditions included a pressure difference across the scaffold and a no-slip wall condition. A typical predicted flow pattern (for the structure of Fig. 5(a)), is shown in Fig. 5(b). As expected, higher flow rates are observed in regions where the structure is more permeable – see Fig. 5(a).

3. Cell architecture characterisation

3.1. Dry scaffolds

The scaffolds used had a relative density ρ^*/ρ_s of 0.5% (porosity content $\sim 99.5\%$), assuming a value of 1.3 Mg m^{-3} for ρ_s [11]. This value is probably an overestimate; such high porosity levels are rather unusual in a material as opposed to a latticework structure. SEM micrographs, such as those illustrated in Fig. 1, suggest that a porosity of around 95% is probably more realistic. It can be seen that the cell walls of the scaffolds are thin (\sim a few microns), as well as being full of apertures (holes and defects). The equivalent cell diameter and cell wall connectivity for the two samples are shown in Fig. 6, as obtained from CT reconstruction analysis. The cell diameter is about $100\text{--}150 \mu\text{m}$ (SEM analysis gave a very similar value for the cell diameter – $119 \pm 73 \mu\text{m}$). The distribution of cell connectivity (aperture size) exhibits a peak at around $20 \mu\text{m}$. There is no systematic difference between CG-1 and CG-2 – the variations just give an indication of sample-to-sample variations. In general, the structure is similar throughout.

3.2. Hydrated scaffolds

The scaffold structure when hydrated – i.e. under conditions close to those *in vivo* – was investigated using 2-photon confocal

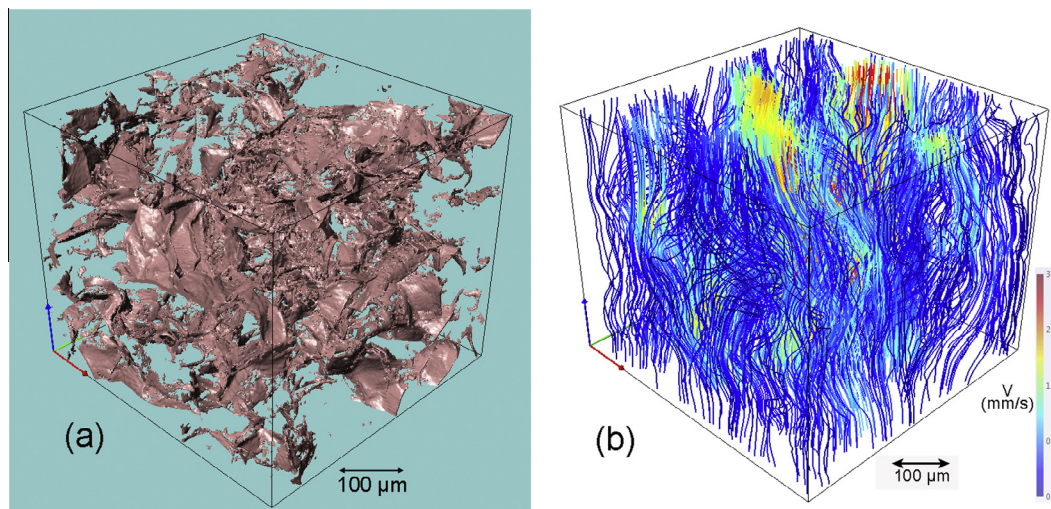


Fig. 5. (a) 3-D tomographic reconstruction of a small volume of a CG scaffold and (b) streamlines for flow of water through this structure under a vertical pressure gradient of 2 Pa mm^{-1} .

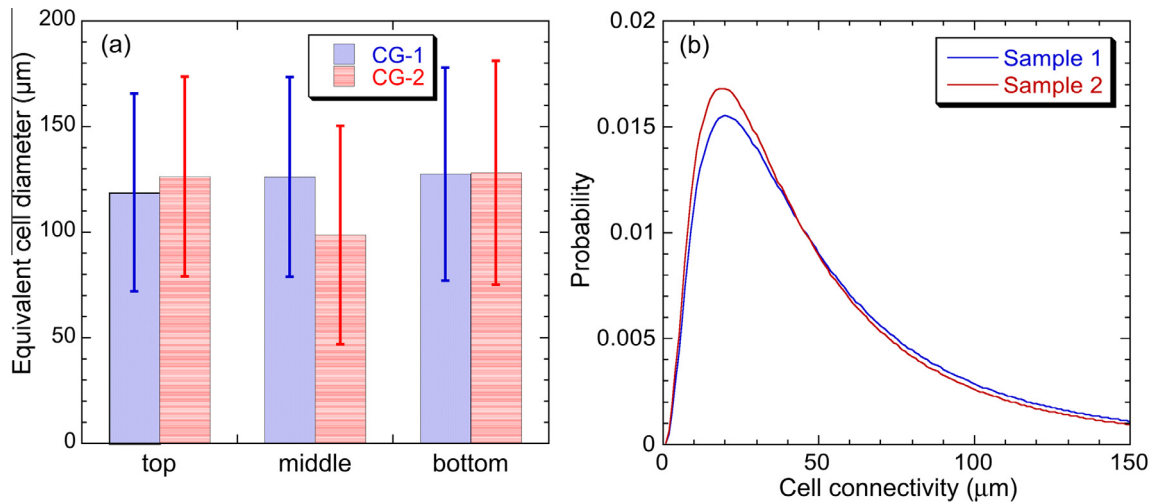


Fig. 6. Structural data for dry scaffolds (2 samples): (a) equivalent cell diameter and (b) cell connectivity (aperture size), as obtained from CT scans. Five sub-sections were analysed from the top, middle and bottom regions (i.e. 15 sub-sections from each sample). Cell diameter is presented as the mean \pm standard deviation. Cell connectivity data are presented as probability distributions.

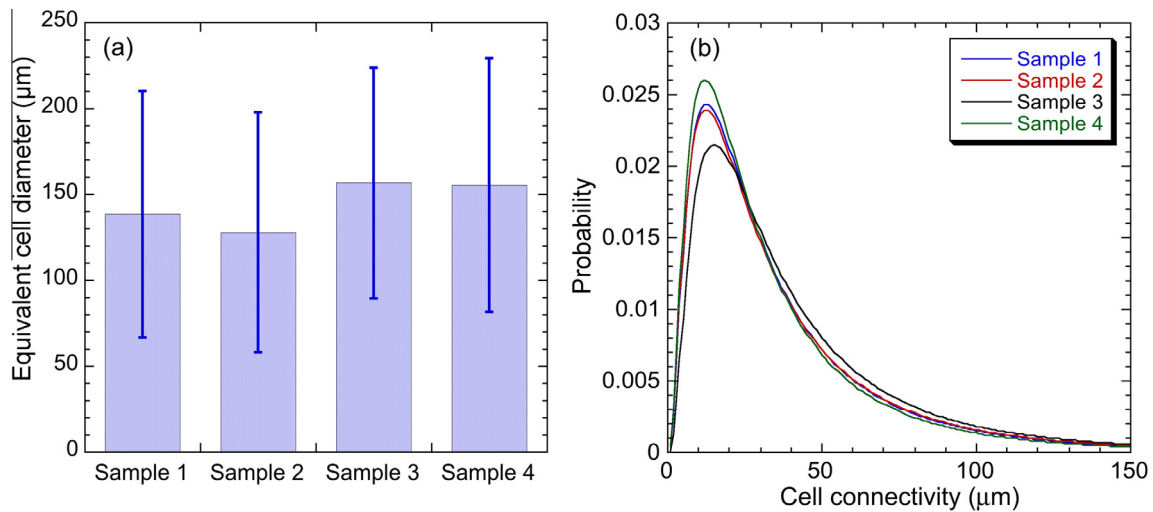


Fig. 7. Structural data for hydrated scaffolds (4 samples): (a) equivalent cell diameter and (b) cell connectivity (aperture size), as obtained from 2-photon microscopy. Cell diameter is presented as the mean \pm standard deviation. Cell connectivity data are presented as probability distributions.

microscopy. Corresponding data to those in Fig. 6 are shown in Fig. 7.

3.3. Specific surface area

Specific surface area values have been obtained using three different techniques. Both the CT tomographic reconstruction analysis and the BET gave a value of about $4 \times 10^4 \text{ m}^{-1}$ for dry scaffolds, while the 2-photon optical reconstruction gave a value of about $3 \times 10^4 \text{ m}^{-1}$ for hydrated scaffolds – see Table II. It is of

Table II

Specific surface areas obtained using BET, and CT and 2-photon reconstruction analyses. Data are presented as the mean \pm standard deviation. (BET: 4 samples, 0.2 g each. CT: 2 samples (15 sub-sections ($1200 \times 1200 \times 250 \mu\text{m}^3$)) from each sample were analysed). 2-photon: 4 samples (1 sub-section ($683.4 \times 683.4 \times 683.4 \mu\text{m}^3$)) from each sample was analysed).

Technique	Specific surface area (10^4 m^{-1})
BET	3.8 ± 1.9
CT tomographic reconstruction	3.8 ± 0.2
2-Photon optical reconstruction	3.0 ± 0.3

note that there is very good agreement between the BET and CT values (both for dry scaffolds), which gives confidence that the order of magnitude is correct.

4. Scaffold properties

4.1. Mechanical properties

Typical compressive stress–strain curves, for dry and hydrated CG scaffolds, are shown in Fig. 8. These were obtained using a standard Instron machine. The curves suggest that, in the hydrated scaffolds, the cell walls tend to buckle and bend at a lower (plateau) stress, compared to the dry scaffolds. Also, the densification strain, above which deformed cell walls start to impinge on each other, is higher for the hydrated scaffolds. Young's modulus values were obtained from the tangent of unloading curves giving $7.6 \pm 0.6 \text{ kPa}$ when dry and $0.57 \pm 0.15 \text{ kPa}$ when hydrated. A typical stress–strain curve showing load–unloading cycles for a dry scaffold, and corresponding inferred Young's modulus values is shown in Fig. 9(a). Using the see-saw testing configuration, the

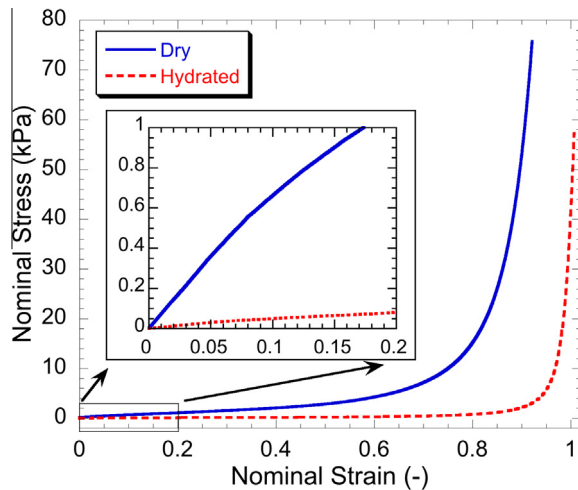


Fig. 8. Typical compressive stress-strain curves for dry and hydrated collagen scaffolds, with an inset showing an expanded view of the low strain region. Three samples from each condition (dry and hydrated) were tested.

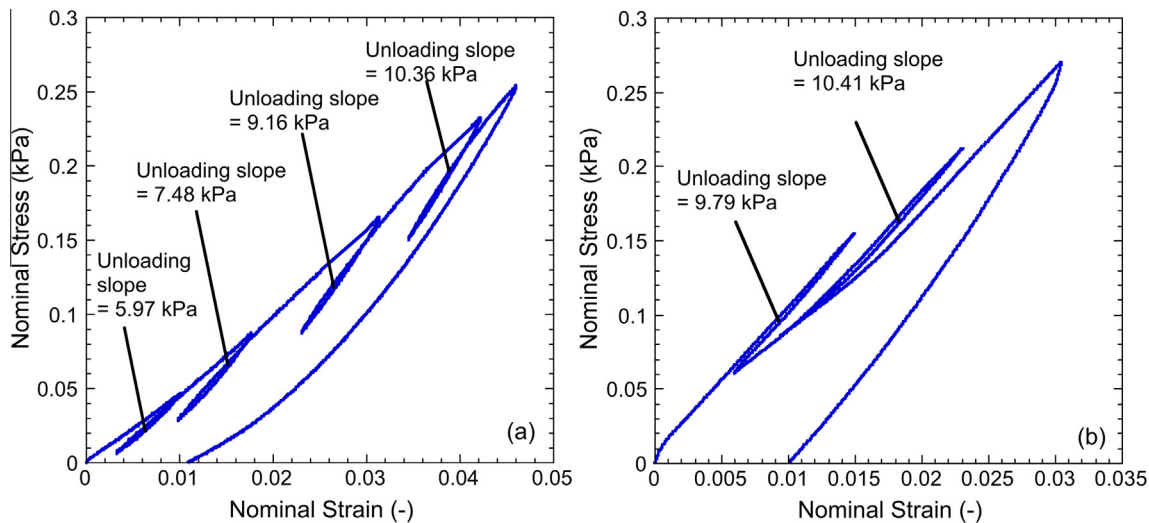


Fig. 9. Load-unloading cycles, and corresponding inferred Young's modulus values, obtained for dry scaffolds tested using (a) conventional testing machine and (b) the customised see-saw set-up. Four samples in both dry and hydrated conditions were tested.

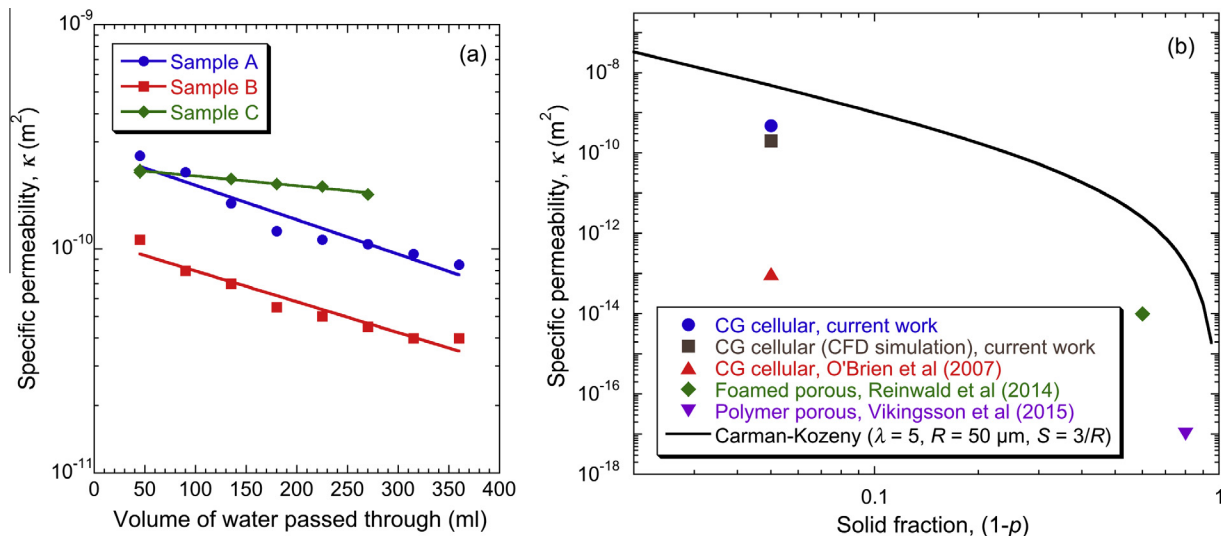


Fig. 10. Measured permeability values (a) as a function of volume of water passed through the sample during testing (3 samples) and (b) compared with experimental results from other studies and with predictions from CFD simulation and the Carman–Kozeny equation.

measured Young's modulus values were 9.6 ± 0.5 kPa when dry and 0.81 ± 0.08 kPa when hydrated. A typical stress-strain curve for a dry scaffold obtained using the see-saw set-up is shown in Fig. 9(b).

4.2. Specific permeability

The average measured value of the specific permeability κ was found to be $4.8 \times 10^{-10} \pm 2.2 \times 10^{-10} \text{ m}^2$. This is in good agreement with predictions based on Computational Fluid Dynamics (CFD) simulation of the flow of water through tomographically-captured structures which gave a value of about $2 \times 10^{-10} \text{ m}^2$. The effect of prolonged flow on the permeability was also assessed. Representative specific permeability data are presented in Fig. 10 (a), which shows values obtained for three different (but nominally the same) scaffolds over an extended period of measurement (about 4 h). It can be seen that there is a tendency for the value to drop after passage of substantial quantities of water through the sample. However, in general the variations are relatively small. This is attributed to scaffold deformation (creep) even under the small pressure gradient applied in this study.

5. Discussion

In the present paper, the cell structure and specific surface area of freeze-dried collagen scaffolds is investigated, in both dry and hydrated states. Measurements are made of their Young's modulus and specific permeability. Young's modulus and permeability are a strong function of porosity level and cell structure. Permeability is also very sensitive to specific surface area. The cell diameter of dry scaffolds is about 100–150 μm and the cell connectivity is about 10–30 μm . These values are consistent with the general impression from Figs. 1 and 2 and show that the cellular structure is a quite heavily disrupted one, with a lot of defects and gaps (apertures) in the walls. By comparing the scaffolds in dry and hydrated states, it can be seen that hydration causes an increase in cell diameter ($\sim 20\%$), while the connectivity has reduced by about 40%. These changes are presumably due to some swelling of the cell walls. In general, however, hydration does not appear to cause any dramatic changes in structure.

CT tomographic reconstruction analysis and BET measurements gave a specific surface area of about $4 \times 10^4 \text{ m}^{-1}$ for dry scaffolds, while 2nd harmonic 2-photon confocal microscopy gave a value of about $3 \times 10^4 \text{ m}^{-1}$ for hydrated scaffolds. These values can't be regarded as highly accurate, but the level of agreement gives confidence that the order of magnitude is correct (and that any change on hydration is relatively small).

The Young's moduli of the scaffolds, in both dry and hydrated states, were measured using conventional mechanical testing and a customised see-saw set-up. As expected, a drop in stiffness was observed on hydration, probably caused by weakening of hydrogen bonds within the molecular structure of the collagen. Fig. 9(a) shows that the Young's modulus value obtained using a conventional Instron machine can vary, depending on the strain at which it is measured. There is a tendency for it to rise with imposed strain, probably due to changes in structure (elastic and/or plastic) that arise as the material is compressed. It can be seen in Fig. 9(b) that this effect was somewhat less pronounced with the see-saw testing configuration, even though the stress and strain ranges concerned were similar. This may be due to the lower inertia of the see-saw set-up, making it easier to interrupt the testing with minimal hysteresis. Furthermore, the see-saw setup is load-controlled (as opposed to conventional loading, which is usually displacement controlled). This means that as the loading increases and the scaffold compresses, the loading platen follows the compression so as to maintain the rate of loading. Load controlled tests are preferred when conducting tests at a very low rate, because an applied load can be kept constant for any given period of time. On the other hand, it can be seen that the values obtained for the Young's modulus ($\sim 5\text{--}10 \text{ kPa}$ for dry and $\sim 0.5\text{--}1 \text{ kPa}$ for hydrated) are similar with the two types of set-up, and values of at least this approximate magnitude have been found in most previous studies [12,13,16,17,21,22,24].

The average measured value of the specific permeability κ was found to be about $5 \times 10^{-10} \text{ m}^2$ which is consistent with predictions based on CFD simulations. This value may be compared with predictions on the Carman–Kozeny equation (Eq. (1)) presented in Section 1. An obvious operation to carry out is to substitute $p = 0.99$, plus some appropriate value of S , into this equation. A very crude estimate of S can be made by approximating the cells in a collagen scaffold to hollow spheres of radius, $R \sim 50 \mu\text{m}$. Assuming the walls to be thin, ignoring the failure of spheres to tessellate and taking only the inner surface to be associated with the sphere concerned:

$$S = \frac{4\pi R^2}{\frac{4}{3}\pi R^3} = \frac{3}{R} \quad (3)$$

corresponding in this case to a value about $6 \times 10^4 \text{ m}^{-1}$. Use of Eq. (1) then gives $\kappa \sim 5 \times 10^{-7} \text{ m}^2$. This is actually a relatively high permeability, which is perhaps unsurprising in view of the porosity level being quite close to 100% – reducing the porosity level to 95% would reduce the permeability by an order of magnitude. However, a substantially lower value is expected with a cellular-type structure, compared with the Carman–Kozeny prediction. In a hollow “cellular” structure of this type, the solid is distributed in such a way as to impede flow rather effectively – in fact, if the cells are all closed, then the permeability is zero. A key question thus relates to cell connectivity – i.e. the presence of holes in cell walls, or the degree to which the structure is genuinely cellular. However, provided there is a reasonable degree of inter-cell connectivity, the above estimate (based on a simple assessment of the area of surface over which the fluid has to flow), while expected to be an overestimate, should not be out by many orders of magnitude.

The only previous study relating to collagen scaffolds of the type being investigated here [10], reports permeability values of 10^{-13} m^2 – i.e. about six orders of magnitude lower than the Carman–Kozeny estimate. This is a very low permeability value, particularly in view of the fact that these scaffolds have a relatively coarse structure and large interconnectivity. Other workers have also obtained very low values, but these relate to scaffolds with lower levels of porosity. For example, Vikingsson et al. [41] obtained values of $\sim 10^{-17} \text{ m}^2$ for polymeric scaffolds containing about 10–30% porosity, while Reinwald et al. [42] obtained 10^{-14} m^2 for supercritical fluid-foamed scaffolds with porosity around 50–60%. It should perhaps be noted in this context that, with very compliant (low stiffness) materials, there must be a concern that the pressure gradients created during permeability measurements may have deformed the structure, perhaps compressing it to such an extent that the permeability dropped dramatically. This could occur even if the deformation were entirely elastic, although obviously plastic deformation might also have occurred. It is noteworthy that the permeability measurements of Lipowiecki et al. [43], carried out on much stiffer and stronger artificial bone scaffolds (although with porosity in the range 30–70% and a broadly similar structural scale and architecture to the materials of Vikingsson et al. [41] and Reinwald et al. [42]), gave values much closer to Carman–Kozeny predictions.

A slightly more systematic comparison with other outcomes is shown in Fig. 10(b), in which specific permeability values are plotted against the solid fraction, $(1 - p)$. Data from three other experimental investigations are included, of which only that by O'Brien et al. [10] was carried out on similar material to that of the current work – the other two studies relating to lower porosity structures that can be considered to contain sets of interconnected pores, rather than being “cellular”. For all four materials, however, the structural scale is similar, since the pores or cells were all about 50 μm in radius. Also shown are predictions from CFD simulation and the Carman–Kozeny equation (Eq. (1)), obtained using $S \sim 3/R$. Of course, this Carman–Kozeny plot does nothing more than provide a very crude guide, and it should be recognised that they are expected to constitute an over-estimate for cellular structures (depending on the cell connectivity). Furthermore, care must be taken when using the Carman–Kozeny equation to predict permeability, since such predictions are highly sensitive to the porosity level, which therefore needs to be known quite accurately. Nevertheless, the three sets of values from previous work do appear to be unexpectedly low, particularly the one for the cellular structure. The most likely explanation for this is that the imposed pressure gradient ($\sim 3 \text{ kPa mm}^{-1}$) in the previous study [10] compressed the structures significantly, reducing the permeability, and there is no doubt that these cellular structures, which are highly compliant ($E \sim 10 \text{ kPa}$), will tend to be susceptible to this effect.

The set-up used in the present work, involving a very low pressure gradient ($\sim 10 \text{ Pa mm}^{-1}$), was specifically designed to reduce this danger. In addition, a press-fit mount was used in contrast to the clamp mount employed in the previous study [10]. The latter caused significant scaffold deformation, reducing the permeability.

6. Conclusions

Collagen scaffolds are used as 3-D platforms for both *in vitro* and *in vivo* studies of cellular interactions and tissue biosynthesis, as well as in clinical repair of a number of tissues. Structure and property characterisation is essential if these scaffolds are to be systematically optimised. This paper outlines a procedure for quantifying the cell structure of freeze-dried collagen scaffolds in both dry and hydrated states using X-ray computed tomography and 2nd harmonic 2-photon confocal microscopy respectively. Measurements have been made of the scaffold's Young's modulus and specific permeability. The freeze-dried collagen scaffolds used in this study have an approximately isotropic cell structure and extensive connectivity between adjacent cells in both dry and hydrated states. This clearly has implications for both the stiffness and the permeability. The scaffold stiffness is very low, about 10 kPa when dry and 1 kPa when hydrated, and these values are consistent with most previous testing of similar scaffolds. There are far fewer data in the literature concerning the specific permeability of collagen scaffolds, but the value reported here is consistent with the CFD simulations, although it is about three orders of magnitude higher than the only previously-reported figure. A likely explanation for this discrepancy is that in the previous work the applied pressure gradient (which was substantially greater than the one employed here) and the scaffold mounting arrangement caused significant compression of the structure, reducing its permeability.

Acknowledgements

This research was supported by the European Research Council (Grant No. 240446) and the EPSRC (EP/E025862/1). Financial support for M.C.V. and R.A.B. has been provided via the WD Armstrong studentship and the National Institute for Health Research (NIHR), respectively.

In compliance with EPSRC requirements, raw data in the form of input files for the CFD simulations (in COMSOL) are available at www.ccg.msm.cam.ac.uk/publications/resources, and are also accessible via the University repository at <http://www.data.cam.ac.uk/repository>.

References

- [1] T.A. Martin, S.R. Caliri, P.D. Williford, B.A. Harley, R.C. Bailey, The generation of biomolecular patterns in highly porous collagen-GAG scaffolds using direct photolithography, *Biomaterials* 32 (2011) 3949–3957.
- [2] Y.Y. Liu, L. Ma, C.Y. Gao, Facile fabrication of the glutaraldehyde cross-linked collagen/chitosan porous scaffold for skin tissue engineering, *Mater. Sci. Eng. C* 32 (2012) 2361–2366.
- [3] M.S. Sader, V.C.A. Martins, S. Gomez, R.Z. LeGeros, G.A. Soares, Production and *in vitro* characterization of 3D porous scaffolds made of magnesium carbonate apatite (MCA)/anionic collagen using a biomimetic approach, *Mater. Sci. Eng. C* 33 (2013) 4188–4196.
- [4] H.F. Shi, X.G. Wang, S.C. Wu, Z.W. Mao, C.G. You, C.M. Han, The effect of collagen–chitosan porous scaffold thickness on dermal regeneration in a one-stage grafting procedure, *J. Mech. Behav. Biomed. Mater.* 29 (2014) 114–125.
- [5] K.H. Shin, J.W. Kim, Y.H. Koh, H.E. Kim, Novel self-assembly-induced 3D plotting for macro/nano-porous collagen scaffolds comprised of nanofibrous collagen filaments, *Mater. Lett.* 143 (2015) 265–268.
- [6] H. Schoof, J. Apel, I. Heschel, G. Rau, Control of pore structure and size in freeze-dried collagen sponges, *J. Biomed. Mater. Res.* 58 (2001) 352–357.
- [7] J.S. Pieper, P.B. van Wachem, M.J.A. van Luyn, L.A. Brouwer, T. Hafmans, J.H. Veerkamp, et al., Attachment of glycosaminoglycans to collagenous matrices modulates the tissue response in rats, *Biomaterials* 21 (2000) 1689–1699.
- [8] S.R. Caliri, B.A. Harley, The effect of anisotropic collagen-GAG scaffolds and growth factor supplementation on tendon cell recruitment, alignment, and metabolic activity, *Biomaterials* 32 (2011) 5330–5340.
- [9] C.M. Murphy, M.G. Haugh, F.J. O'Brien, The effect of mean pore size on cell attachment, proliferation and migration in collagen-glycosaminoglycan scaffolds for bone tissue engineering, *Biomaterials* 31 (2010) 461–466.
- [10] F.J. O'Brien, B.A. Harley, M.A. Waller, I.V. Yannas, L.J. Gibson, P.J. Prendergast, The effect of pore size on permeability and cell attachment in collagen scaffolds for tissue engineering, *Technol. Health Care* 15 (2007) 3–17.
- [11] F.J. O'Brien, B.A. Harley, I.V. Yannas, L.J. Gibson, The effect of pore size on cell adhesion in collagen-GAG scaffolds, *Biomaterials* 26 (2005) 433–441.
- [12] B.A. Harley, J.H. Leung, E.C. Silva, L.J. Gibson, Mechanical characterization of collagen-glycosaminoglycan scaffolds, *Acta Biomater.* 3 (2007) 463–474.
- [13] B.P. Kanungo, L.J. Gibson, Density-property relationships in mineralized collagen-glycosaminoglycan scaffolds, *Acta Biomater.* 5 (2009) 1006–1018.
- [14] B.P. Kanungo, L.J. Gibson, Density-property relationships in collagen-glycosaminoglycan scaffolds, *Acta Biomater.* 6 (2010) 344–353.
- [15] V.A. Santamaria, H. Deplaine, D. Mariggio, A.R. Villanueva-Molines, J.M. Garcia-Aznar, J.L.G. Ribelles, et al., Influence of the macro and micro-porous structure on the mechanical behavior of poly(L-lactic acid) scaffolds, *J. Non-Cryst. Solids* 358 (2012) 3141–3149.
- [16] D.W. Weisgerber, D.O. Kelkhoff, S.R. Caliri, B.A. Harley, The impact of discrete compartments of a multi-compartment collagen-GAG scaffold on overall construct biophysical properties, *J. Mech. Behav. Biomed. Mater.* 28 (2013) 26–36.
- [17] B.P. Kanungo, E. Silva, K. Van Vliet, L.J. Gibson, Characterization of mineralized collagen-glycosaminoglycan scaffolds for bone regeneration, *Acta Biomater.* 4 (2008) 490–503.
- [18] F.J. O'Brien, Influence of freezing rate on pore structure in freeze-dried collagen-GAG scaffolds, *Biomaterials* 25 (2004) 1077–1086.
- [19] M. Madaghiele, A. Sannino, I.V. Yannas, M. Spector, Collagen-based matrices with axially oriented pores, *J. Biomed. Mater. Res., Part A* 85A (2008) 757–767.
- [20] N. Davidenko, T. Gibb, C. Schuster, S.M. Best, J.J. Campbell, C.J. Watson, et al., Biomimetic collagen scaffolds with anisotropic pore architecture, *Acta Biomater.* 8 (2012) 667–676.
- [21] M.G. Haugh, C.M. Murphy, R.C. McKiernan, C. Altenbuchner, F.J. O'Brien, Crosslinking and mechanical properties significantly influence cell attachment, proliferation, and migration within collagen glycosaminoglycan scaffolds, *Tissue Eng. Part A* 17 (2011) 1201–1208.
- [22] C.M. Tierney, M.G. Haugh, J. Liedl, F. Mulcahy, B. Hayes, F.J. O'Brien, The effects of collagen concentration and crosslink density on the biological, structural and mechanical properties of collagen-GAG scaffolds for bone tissue engineering, *J. Mech. Behav. Biomed. Mater.* 2 (2009) 202–209.
- [23] M.B. Keogh, F.J. O'Brien, J.S. Daly, Substrate stiffness and contractile behaviour modulate the functional maturation of osteoblasts on a collagen-GAG scaffold, *Acta Biomater.* 6 (2010) 4305–4313.
- [24] C.M. Murphy, A. Matsiko, M.G. Haugh, J.P. Gleeson, F.J. O'Brien, Mesenchymal stem cell fate is regulated by the composition and mechanical properties of collagen-glycosaminoglycan scaffolds, *J. Mech. Behav. Biomed. Mater.* 11 (2012) 53–62.
- [25] C.T.J. Dodson, W.W. Sampson, Spatial statistics of stochastic fiber networks, *J. Stat. Phys.* 96 (1999) 447–458.
- [26] X.F. Wu, Y.A. Dzenis, Elasticity of planar fiber networks, *J. Appl. Phys.* 98 (2005) 093501.
- [27] A.E. Markaki, T.W. Clyne, Magneto-mechanical actuation of bonded ferromagnetic fibre arrays, *Acta Mater.* 53 (2005) 877–889.
- [28] T.W. Clyne, A.E. Markaki, J.C. Tan, Mechanical and magnetic properties of metal fibre networks, with and without a polymeric matrix, *Compos. Sci. Technol.* 65 (2005) 2492–2499.
- [29] D.N. Woolfson, Building fibrous biomaterials from alpha-helical and collagen-like coiled-coil peptides, *Biopolymers* 94 (2010) 118–127.
- [30] M.F. Hadi, V.H. Barocas, Microscale fiber network alignment affects macroscale failure behavior in simulated collagen tissue analogs, *J. Biomech. Eng. Trans. ASME* 135 (2013).
- [31] C.B. da Cunha, D.D. Klumpers, W.A. Li, S.T. Koshy, J.C. Weaver, O. Chaudhuri, et al., Influence of the stiffness of three-dimensional alginate/collagen-I interpenetrating networks on fibroblast biology, *Biomaterials* 35 (2014) 8927–8936.
- [32] A. D'Amore, N. Amoroso, R. Gottardi, C. Hobson, C. Carruthers, S. Watkins, et al., From single fiber to macro-level mechanics: a structural finite-element model for elastomeric fibrous biomaterials, *J. Mech. Behav. Biomed. Mater.* 39 (2014) 146–161.
- [33] B. Marelli, C.E. Ghezzi, M. James-Bhasin, S.N. Nazhat, Fabrication of injectable, cellular, anisotropic collagen tissue equivalents with modular fibrillar densities, *Biomaterials* 37 (2015) 183–193.
- [34] T.S. Karande, J.L. Ong, C.M. Agrawal, Diffusion in musculoskeletal tissue engineering scaffolds: design issues related to porosity, permeability, architecture, and nutrient mixing, *Ann. Biomed. Eng.* 32 (2004) 1728–1743.
- [35] G. Ahn, J.H. Park, T. Kang, J.W. Lee, H.W. Kang, D.W. Cho, Effect of pore architecture on oxygen diffusion in 3D scaffolds for tissue engineering, *J. Biomech. Eng. Trans. ASME* 132 (2010).
- [36] A.G. Mitsak, J.M. Kemppainen, M.T. Harris, S.J. Hollister, Effect of polycaprolactone scaffold permeability on bone regeneration *in vivo*, *Tissue Eng. Part A* 17 (2011) 1831–1839.

- [37] S.M. Giannitelli, D. Accoto, M. Trombetta, A. Rainer, Current trends in the design of scaffolds for computer-aided tissue engineering, *Acta Biomater.* 10 (2014) 580–594.
- [38] V. Bhaaerath, J. Venugopal, C. Gandhimathi, N. Ponpandian, D. Mangalaraj, S. Ramakrishna, Biologically improved nanofibrous scaffolds for cardiac tissue engineering, *Mater. Sci. Eng. C* 44 (2014) 268–277.
- [39] F.J. Valdes-Parada, J.A. Ochoa-Tapia, J. Alvarez-Ramirez, Validity of the permeability Carman–Kozeny equation: a volume averaging approach, *Phys. A Stat. Mech. Appl.* 388 (2009) 789–798.
- [40] F. Pennella, G. Cerino, D. Massai, D. Gallo, G.F.D. Labate, A. Schiavi, et al., A survey of methods for the evaluation of tissue engineering scaffold permeability, *Ann. Biomed. Eng.* 41 (2013) 2027–2041.
- [41] L. Vikingsson, B. Claessens, J.A. Gomez-Tejedor, G.G. Ferrer, J.L.G. Ribelles, Relationship between micro-porosity, water permeability and mechanical behavior in scaffolds for cartilage engineering, *J. Mech. Behav. Biomed. Mater.* 48 (2015) 60–69.
- [42] Y. Reinwald, R.K. Johal, A.M. Ghaemmaghami, F. Rose, S.M. Howdle, K.M. Shakesheff, Interconnectivity and permeability of supercritical fluid-foamed scaffolds and the effect of their structural properties on cell distribution, *Polymer* 55 (2014) 435–444.
- [43] M. Lipowiecki, M. Ryvolova, A. Tottosi, N. Kolmer, S. Naher, S.A. Brennan, et al., Permeability of rapid prototyped artificial bone scaffold structures, *J. Biomed. Mater. Res., Part A* 102 (2014) 4127–4135.